

# A Spherical Brain Mapping of MR Images for the Detection of Alzheimer's Disease.

F.J. Martinez-Murcia, J.M. Górriz\*, J. Ramírez  
Dept. of Signal Theory, Networking and Communications  
18071 University of Granada, Spain

A. Ortiz  
Dpt. of Communications Engineering  
29071 University of Málaga, Spain

for the Alzheimer's Disease Neuroimaging Initiative<sup>†</sup>

## Abstract

*Magnetic Resonance Imaging (MRI) is of fundamental importance in neuroscience, providing good contrast and resolution, as well as not being considered invasive. Despite the development of newer techniques involving radiopharmaceuticals, it is still a recommended tool in Alzheimer's Disease (AD) neurological practice to assess neurodegeneration, and recent research suggests that it could reveal changes in the brain even before the symptomatology appears. In this paper we propose a method that performs a Spherical Brain Mapping, using different measures to project the three-dimensional MR brain images onto two-dimensional maps revealing statistical characteristics of the tissue. The resulting maps could be assessed visually, but also perform a significant feature reduction that will allow further supervised or unsupervised processing, reducing the computational load while maintaining a large amount of the original information. We have tested our methodology against a MRI database comprising 180 AD affected patients and 180 normal controls, where some of the mappings have revealed as an optimum strategy for the automatic processing and characterization of AD patterns, achieving up to a 90.9% of accuracy, as well as significantly reducing the computational load. Additionally, our maps allow the visual analysis and interpretation of the images, which can be of great help in the diagnosis of this and other types of dementia.*

## I. INTRODUCTION

Alzheimer's Disease (AD) is currently the most common neurodegenerative disease in the world, with more than 44.4 million affected people, and it is likely to have increased up to 135.5 million by 2050. According to research, most people currently living with this type of dementia have not received a formal diagnosis [1]. In this task, the development of medical imaging has represented a major breakthrough, allowing the physicians to explore a number of structural and functional biomarkers that previously could only be accessed post-mortem.

---

\*Corresponding author: [gorriz@ugr.es](mailto:gorriz@ugr.es)

<sup>†</sup>Data used in preparation of this article were obtained from the Alzheimer's Disease Neuroimaging Initiative (ADNI) database ([adni.loni.usc.edu](http://adni.loni.usc.edu)). As such, the investigators within the ADNI contributed to the design and implementation of ADNI and/or provided data but did not participate in analysis or writing of this report. A complete listing of ADNI investigators can be found at: [http://adni.loni.usc.edu/wp-content/uploads/how\\_to\\_apply/ADNI\\_Acknowledgement\\_List.pdf](http://adni.loni.usc.edu/wp-content/uploads/how_to_apply/ADNI_Acknowledgement_List.pdf)

Recently, a number of very specific radiopharmaceuticals, such as Pittsburgh compound B (PiB), a radioactive analog of thioflavin T that binds to fibrillar amyloid-beta ( $A\beta$ ), have been developed. However, their invasive nature and their technical requirements -specially when the half-life of the radioactive element is usually low, and therefore, its synthesis requires a nearby cyclotron- make them unusual in the clinical practice. Conversely, Magnetic Resonance Imaging (MRI) is a more widespread technique that allows the characterization of brain atrophy, and accordingly, is far more established in clinical practice.

Therefore, MR brain images have been extensively used in the diagnosis of AD by assessing neurodegeneration on grey matter (GM) and White Matter (WM) tissues. Research has shown in [2, 3, 4, 5] that neurodegeneration in Alzheimer's Disease mainly occurs in the GM tissue. Particularly grey matter loss has been described in the Hippocampus and Parahippocampal lobes, according to the NINCDS-ADRDA criteria for AD diagnosis [5], with further atrophy described in the medial temporal structures, the Posterior Cingulate gyrus and adjacent Precuneus [2]. Moreover, significantly lower volumes of certain regions in GM and WM have been considered a promising biomarker and predictor of the progression of AD in a longitudinal study involving Mild Cognitive Impairment (MCI) patients [3], and some structures in the striatum (putamen and caudate nucleus) have shown important volume abnormalities [4]. All these data suggest that many of the symptoms of AD can be observed in anatomical MR images even in early stages of the disease, which could be of great help in its successful diagnosis and treatment.

Notwithstanding the utility of MRI, the task of examining the images currently depends on several qualitative or semi-quantitative analyses, and relies often on the examiner's subjectivity [6]. Therefore, the development of objective, quantitative automatic methods is desirable. For this purpose, a number of statistical tools and algorithms have been developed, leading to what is known as the Computer Aided Diagnosis (CAD) paradigm. A large number of analysis rely on univariate approaches, using SVM and Voxels As Features [6] or the processing of different Regions of Interest (ROIs) [7, 8], along with the statement of specific anatomical biomarkers to predict AD, like cortical thickness [9, 10]. Other multivariate approaches, which consider the brain as a whole, have been proposed in the literature, either using component-based methods [11, 12, 13, 14] or different classification approaches [15, 16, 17]. Most approaches to this task imply the addition of a priori knowledge about the different areas in the brain, and its subsequent study, obtaining high accuracy in the detection of the disease [7, 13].

The main aim of this work is to provide a new framework that allows the mapping of a 3D brain image to a two-dimensional space by means of some statistical measures [18]. The system is based on a conversion from 3D spherical to 2D rectangular coordinates. For each spherical coordinate pair  $(\theta, \varphi)$ , a vector containing all voxels in the radius is selected, and a number of values are computed, including statistical values (average, entropy, kurtosis) and morphological values (tissue thickness, distance to the central point, number of non-zero blocks). These values conform a two-dimensional image that can be computationally or even visually analysed. In this paper, we proceed using an statistical mask computed using a two-sample  $t$ -Test, and a SVM classifier. We have achieved performance results that match those obtained with a priori information but using a complete automated procedure, which furthermore reduces the dimensionality of the original images from more than two million voxels to hardly tens of thousands pixels. These maps can be successfully used by itself, but also allow further processing by using them combined and applying some univariate or multivariate algorithms for dimensional reduction.

Figure 1 gives an overview of the procedure used in this article. First, the MRI T1 brain images are segmented, and mapped onto two dimensions using our proposed Statistical Brain Mapping algorithm (see Sec. II.2). Then, the most relevant voxels, according to the  $t$ -values obtained by a two-sample  $t$ -Test, are selected (Sec. II.5) and a feature vector is constructed with them. Finally,

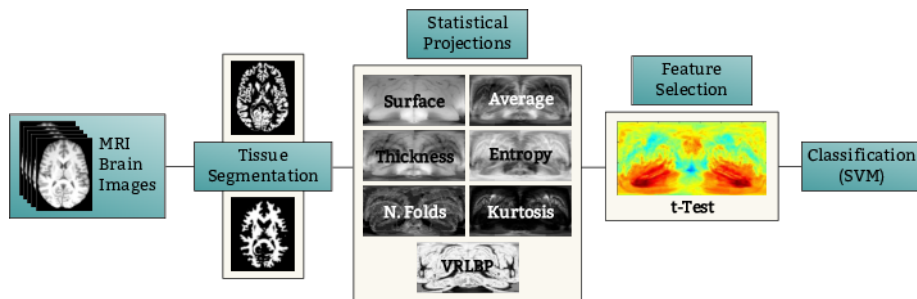


**Figure 1:** Flow diagram of the procedure used in the textural analysis of projected MR brain images.

we train and test a SVM classifier in a AD vs not AD (normal controls, NC) paradigm to assess the ability of our 2D mappings in the detection of Alzheimer’s Disease.

## II. MATERIALS AND METHODS

### II.1. MRI Brain Image database

Data used in the preparation of this article were obtained from the Alzheimer’s Disease Neuroimaging Initiative (ADNI) database ([adni.loni.usc.edu](http://adni.loni.usc.edu)). The ADNI was launched in 2003 as a public-private partnership, led by Principal Investigator Michael W. Weiner, MD. The primary goal of ADNI has been to test whether serial magnetic resonance imaging (MRI), positron emission tomography (PET), other biological markers, and clinical and neuropsychological assessment can be combined to measure the progression of mild cognitive impairment (MCI) and early Alzheimer’s disease (AD).

The database used in this article was extracted from the ADNI1: Screening 1.5T (subjects who have a screening data) and contains 1075 T1-weighted MR images (for further information, see [www.adni-info.org](http://www.adni-info.org)).

In this work, a total number of 360 individuals (180 AD and 180 NC) have been randomly selected to avoid class prevalence. The images were preprocessed, co-registered and segmented using the Statistical Parametric Mapping (SPM) software [19], and the Voxel-Based-Morphometry 8 (VBM8) toolbox [20]. First, the preprocessing was performed using a nonlinear deformation field using the tissue probability maps provided by the International Consortium for Brain Mapping (ICBM). Secondly, we affine registered the data to the Montreal Neurological Institute (MNI) space and resized to  $121 \times 145 \times 121$  voxel. Later, we performed the co-registration using the high-dimensional Dartel normalization using the standard Dartel template provided by VBM8. Finally, the images were segmented using VBM8 again, yielding probability maps that consist of values in the range  $(0, 1)$  for each voxel. These values estimate each voxel’s membership probability (WM, GM or Cerebro-Spinal Fluid), although CSF maps were not used in our experiments.

### II.2. Spherical Brain Mapping

The technique proposed to perform the mapping of the 3D brain images to a 2D map using spherical coordinates -from now on Spherical Brain Mapping (SBM)- is based on the use of spherical coordinates in the brain. A base point is set in the central voxel of the MRI image, and a mapping vector  $\mathbf{v}_i$  of length  $N$  is defined for each inclination ( $\theta$ ) and azimuth ( $\varphi$ ) angles in the range  $0^\circ < \theta < 180^\circ$  and  $0^\circ < \varphi < 360^\circ$  (see Figure 2). Therefore, we will define the sampled set

$V_{\theta,\varphi}$ , a set that contains  $P$  voxels crossed by the sampling vector  $\mathbf{v}_i$ . For each set  $\mathbf{v}_i$ , a mapping value  $v$  is computed from the sampled voxels  $V_{\theta,\varphi}$ , depending on the measure used. In this section, six basic measures are proposed:

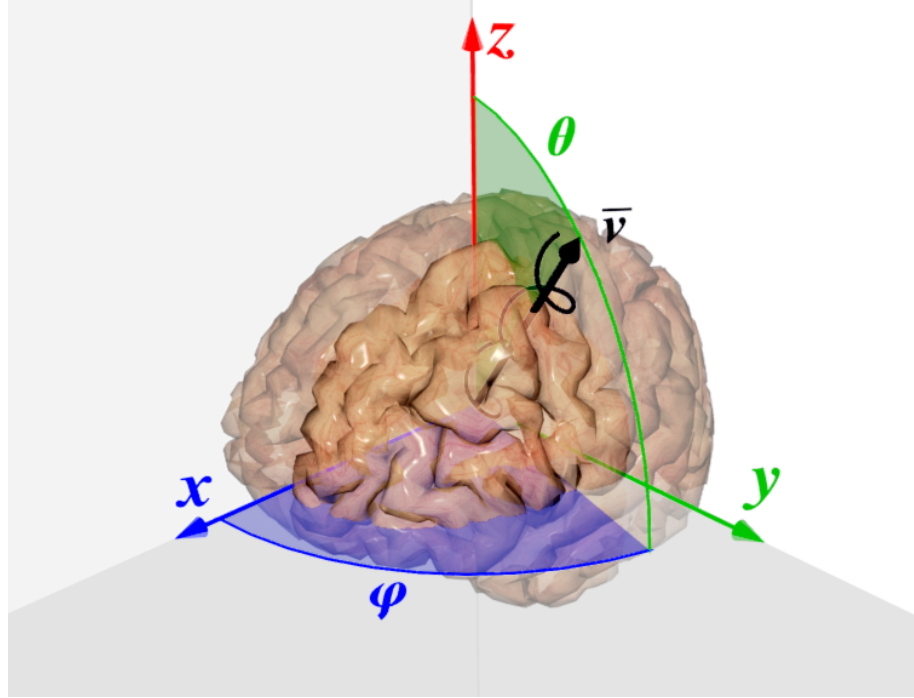


**Figure 2:** Illustration of the computation of the mapping vector  $\mathbf{v}_i$ , the angles  $\theta$  and  $\varphi$  and the  $r$ -neighbourhood of  $\mathbf{v}$  (see Section II.4).

- A basic brain surface approach, that accounts for the distance between the central voxel and the last tissue voxel in  $V_{\theta,\varphi}$  that is greater than a threshold  $I_{th}$ . This might allow our system to observe structural degeneration and tissue loss in the surface of the tissue.

$$v_{surf} = \arg \max_i \{V_{\theta,\varphi}(i) > I_{th}\} \quad \forall i = 1, \dots, P \quad (1)$$

- Another parameter used is thickness of the tissue. This can be useful when measuring the thickness of segmented Gray Matter or White Matter MR images. It is defined as the distance between the last and first elements in  $V_{\theta,\varphi}$  with an intensity greater than a threshold  $I_{th}$  (typically 0):

$$v_{thick} = \arg \max_i \{V_{\theta,\varphi}(i) > I_{th}\} - \arg \min_i \{V_{\theta,\varphi}(i) > I_{th}\} \quad \forall i = 1, \dots, P \quad (2)$$

- The number of folds represents the number of overlapping segments of tissue in the set  $V_{\theta,\varphi}$ . It is computed by thresholding  $V_{\theta,\varphi}$  using the value  $I_{th}$  and counting the number of resulting connected subsets. Let  $A_{\theta,\varphi}$  be the set that contains all the indices of the voxels in  $V_{\theta,\varphi}$  with an intensity greater than  $I_{th}$ :

$$A_{\theta,\varphi} = \{i / V_{\theta,\varphi}(i) > I_{th}\} \quad (3)$$

where  $A_{\theta,\varphi} \in \mathbb{N}$ . Let us divide  $A_{\theta,\varphi}$  in  $J$  disjoint connected subsets so that:

$$A_{\theta,\varphi} = A_{\theta,\varphi}^1 \cup A_{\theta,\varphi}^2 \cup \dots \cup A_{\theta,\varphi}^J \quad \text{so that} \quad A_{\theta,\varphi}^i \cap A_{\theta,\varphi}^j = \emptyset \quad \forall i, j \quad (4)$$

Therefore, our  $v_{nf} = J$ , the number of disjoint connected subsets in  $A_{\theta,\varphi}$ .

- An average approach, where the average of all the intensity values in the set  $V_{\theta,\varphi}$  is computed as:

$$v_{av} = \frac{1}{N} \sum_i V_{\theta,\varphi}(i) \quad \forall i = 1, \dots, P \quad (5)$$

- The entropy assumes that the set  $V_{\theta,\varphi}$  is a probability mass vector (probability of belonging to a certain tissue, normalized) and computes  $v$  as:

$$v_{ent} = \sum_i V_{\theta,\varphi}(i) * \log(V_{\theta,\varphi}(i)) \quad \forall i \in \arg_i\{V_{\theta,\varphi}(i) > 0\} \quad (6)$$

- The uncorrected kurtosis, also known as fourth standardized moment, of the set  $V_{\theta,\varphi}$  in which  $v$  is calculated using:

$$v_{kurt} = \frac{\frac{1}{N} \sum_i (V_{\theta,\varphi}(i) - \bar{V}_{\theta,\varphi}(i))^4}{\left(\frac{1}{N} \sum_i (V_{\theta,\varphi}(i) - \bar{V}_{\theta,\varphi}(i))^2\right)^2} \quad \forall i = 1, \dots, P \quad (7)$$

where  $\bar{V}_{\theta,\varphi}$  is the average of all voxels in  $V_{\theta,\varphi}$  (same value as  $v_{av}$ , described in Eq. 5).

The resulting GM and WM maps are depicted in Figure 3.

The resulting maps will contain the value  $v$  mapped in each direction  $(\theta, \varphi)$ . As the inclination angle  $\theta$  ranges from  $0^\circ$  to  $180^\circ$  and the azimuth  $\varphi$  from  $0^\circ$  to  $360^\circ$ , the resulting maps will have a size of  $181 \times 361$ , where each pixel is the  $v$  value for each direction. The whole algorithm can be downloaded at <http://wdb.ugr.es/~fjesusmartinez/portfolio/sbm/>.

This methodology defines the sampling set as the voxels that are crossed by the sampling vector  $\mathbf{v}_{\theta,\varphi}$ . When projecting a structure as complex as the brain, this implies a loss of contextual information of both the neighbourhood and the layers crossed by  $\mathbf{v}_{\theta,\varphi}$ . Two approaches have been suggested to overcome this problem: the first one extends the system by dividing the sampling set  $V_{\theta,\varphi}$  in  $n$  equal parts in a so-called ‘‘Layered approach’’, and the second one uses a helical sampling and Local Binary Patterns (LBP) to map the neighbourhood of the sampling vector and characterize the texture of the area.

### II.3. Layered Extension

The first strategy used to improve the descriptive abilities of the mappings is the Layered Extension. In this approach, the sampled voxels set  $V_{\theta,\varphi}$  can be divided in  $n$  equal subsets, using each one to project one section -or layer- of the brain. If, for example, we use  $n = 4$ , 4 subsets containing the same number of voxels will be derived from  $V_{\theta,\varphi}$ , and therefore 4 different maps will be depicted, from the closest to the centre to the farthest. This layered approach reveals the different anatomical structures found in the brain at different depths, potentially revealing a more detailed distribution the features of the mappings . These layered maps and their performance will be discussed later.

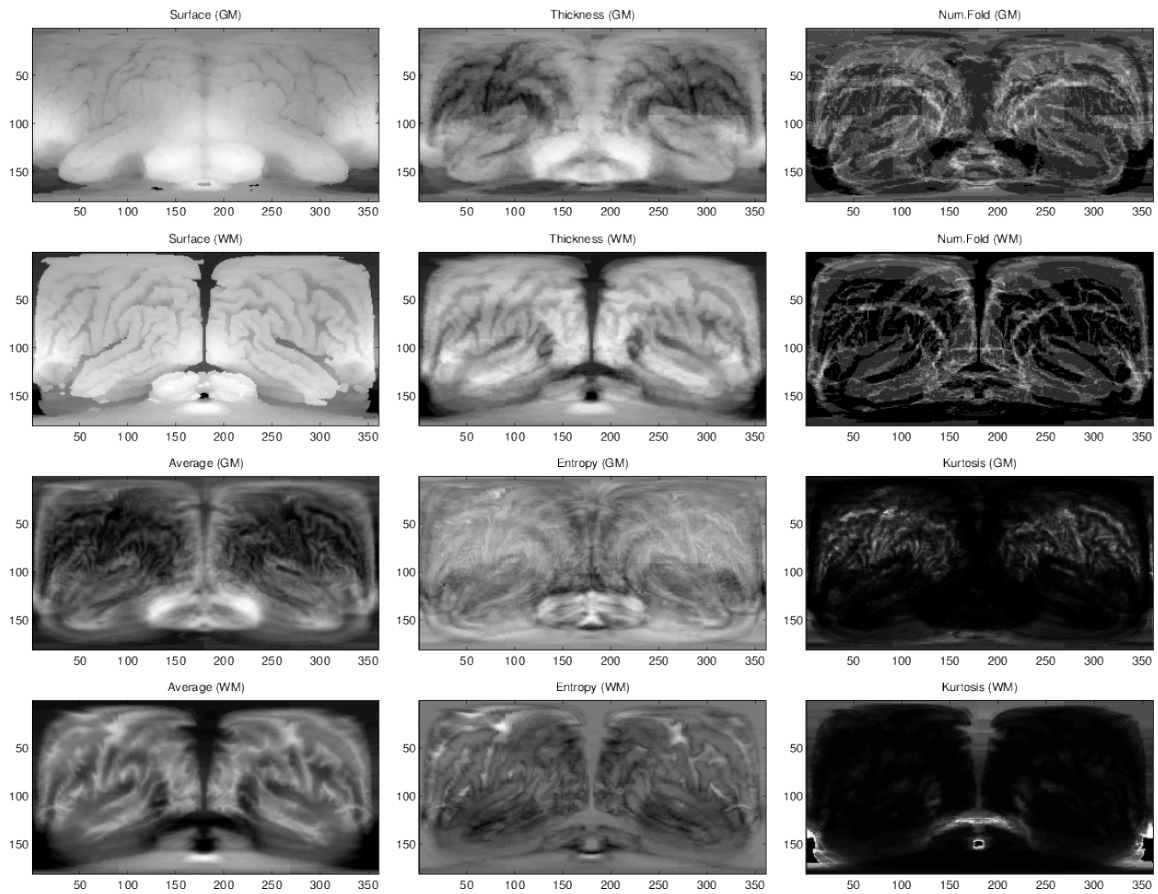


**Figure 3:** Resulting GM and WM maps of the same control subject using the six proposed measures: Surface, Thickness, Number of Folds, Average, Entropy and Kurtosis.

## II.4. SBM based on Local Binary Patterns

In a second attempt to overcome the loss of per layer information, we have expanded the influence of  $\mathbf{v}_{\theta,\varphi}$  to its  $r$ -neighbourhood. This has been done by defining a  $v$  measure that describes not only the features of the voxels crossed by  $\mathbf{v}_{\theta,\varphi}$ , but the texture of its neighbourhood using a Volumetric Radial Volumetric Radial Local Binary Pattern (VRLBP) descriptor.

Local Binary Patterns (LBP) were first introduced in [21] to describe the texture of an image with application to face recognition. Later, in [22], the technique was extended to a Volume LBP (VLBP), defining a 3D texture in a local neighbourhood by using a cylinder oriented in one direction and whose radius define the neighbourhood used to compute the LBP descriptor.

In the VRLBP, the sampling method devised in [22] has been updated to follow helical coordinates around the mapping vector  $\mathbf{v}_{\theta,\varphi}$  (see helix around  $\mathbf{v}_{\theta,\varphi}$  in Figure 2). Formally, we note  $V_{\theta,\varphi}^{P,r}$  the set of  $P$  sampled voxels of the image  $I$  in the  $r$ -neighbourhood of  $\mathbf{v}_{\theta,\varphi}$  taken by helical sampling:

$$V_{\theta,\varphi}^{P,r} = \{I(g_{\theta,\varphi}^{0,r}), I(g_{\theta,\varphi}^{1,r}), I(g_{\theta,\varphi}^{2,r}), \dots, I(g_{\theta,\varphi}^{P-1,r})\} \quad (8)$$

where the coordinates  $g_{\theta,\varphi}^{p,r}$  of each voxel are computed in the direction of  $\mathbf{v}_{\theta,\varphi}$  by:

$$g_{\theta,\varphi}^{p,r} = \begin{cases} x_{\theta,\varphi}^{p,r} = p \sin(\varphi) \cos(\theta) - r \sin(2\pi n \frac{p}{P}) \\ y_{\theta,\varphi}^{p,r} = p \sin(\varphi) \sin(\theta) + r \cos(2\pi n \frac{p}{P}) \\ z_{\theta,\varphi}^{p,r} = p \cos(\varphi) \end{cases} \quad p = \{0, \dots, P-1\}, P \in \mathbb{N} \quad (9)$$

being  $n$  the number of loops in the helix. Following [22], voxels that do not fall exactly at the coordinates computed in the equations 9 are estimated by interpolation.

Let us assume, without loss of generality, that  $P$  and  $r$  are fixed. This way, set of sampled voxels  $V_{\theta,\varphi}^{P,r}$  becomes  $V_{\theta,\varphi}$ , which matches the definition of Section II.2. Following this notation, the value  $v$  for this VRLBP approach is computed using:

$$v_{VRLBP} = \sum_i s(V_{\theta,\varphi}(i) - V_{\theta,\varphi}(0)) \cdot 2^i \quad \forall i = 1, \dots, P \quad (10)$$

where  $s(x)$  is the sign function, defined as:

$$s(x) = \begin{cases} 1 & x \geq 0 \\ 0 & x < 0 \end{cases} \quad (11)$$

This approach provides textural information about all brain structures in a certain direction, as it can be seen in Figure 4.

## II.5. Feature Selection

For a further dimensionality reduction, and pixel relevance assessment, we can proceed as in [14], by selecting the most descriptive voxels according to a criterium. In this case, we will use the two-sample  $t$ -Test with pooled variance estimate. To do so, we define the vector  $\mathbf{s}_C$  that contains all values  $v$  of a certain pixel along all maps belonging to a class  $C$ . Hence, a  $t$ -value is computed for each pixel in our maps:

$$t = \frac{|\bar{\mathbf{s}}_1 - \bar{\mathbf{s}}_0|}{\sqrt{\frac{\hat{\sigma}_{\mathbf{s}}^2}{N_1} + \frac{\hat{\sigma}_{\mathbf{s}}^2}{N_0}}} \quad (12)$$

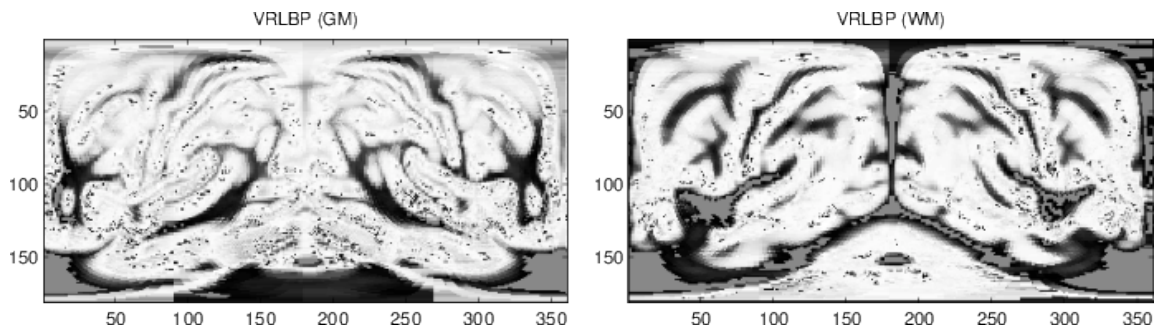


**Figure 4:** An example of the VRLBP projection for GM and WM Tissues.

In our experimental setup, once this  $t$ -value has been computed for all pixels in the map, we rank the pixels from highest to lowest  $t$ -value. Finally, a percentage of the most relevant features is selected as the feature vector that characterizes that image.

### III. RESULTS

#### III.1. Experimental settings and validation

In this work, we have considered a binary classification problem: AD vs. NC, where we have evaluated separately each type of mapping. First, in Section III.2, we will analyse our maps by means of the  $t$  statistic, where the areas of higher statistical significance (AD vs NC) will be highlighted. To better interpret the results, an anatomical reference is provided.

Second, we have performed a classification analysis using feature selection by means of  $t$ -Test, then training and testing a linear SVM classifier. The method has been validated using stratified 10-fold cross-validation, as recommended in [23]. This procedure consists on randomly partitioning the whole datasets into 10 subsets that contain the same proportion of individual of both classes as the whole database. Then, one subset is used for testing and the remaining 9 are used for training. This is repeated for each of the subsets as training sets. Finally, the whole cross-validation strategy will be repeated 10 times to avoid the possible bias and random effects of the partitions, and obtain the average and standard deviation of the performance values.

Values of accuracy (acc), sensitivity (sens) and specificity (spec) along with their standard deviation will be employed to evaluate the performance of the different mappings. Selection of parameter  $C$  of the SVM classifier (as implemented in LIBSVM [24]) will be performed using an inner 5-fold cross-validation on the training subset.

#### III.2. Statistical Significance Analysis

In this section, we will study the statistical significance of the SBM maps by using a two-sample  $t$ -Test with pooled variance estimate, as defined in Section II.5. The computed  $t$  values for each coordinate pair in the maps  $(\theta, \varphi)$  will be displayed later in Section III.2.2 for the six original measures, in Section III.2.3 for the layered extension and in Section III.2.4 for the VRLBP. However, to provide a better understanding of these  $t$ -maps, an anatomical reference is provided in Section III.2.1.

### III.2.1 Anatomical Reference

Our SBM technique maps all sampled voxels selected by our mapping vector  $v_{\theta,\varphi}$  to a single point in the projected map. These points cross different anatomical regions, however it is difficult to know at first which regions are crossed, given the coordinate pairs  $(\theta, \varphi)$ . To clarify this and provide a better understanding, we have mapped the widely known Automated Anatomical Labeling (AAL) [25] map using SBM, and the regions are displayed in Figures 5 and 6.

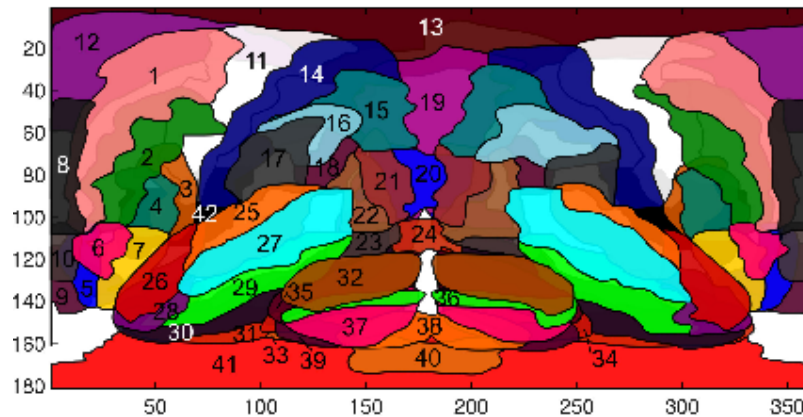


**Figure 5:** Projection of different cortical regions. In the Frontal region, we can find: 1) Frontal Sup., 2) Frontal Mid., 3) Frontal Inf. Oper., 4) Frontal Inf. Tri., 5) Frontal Sup. Orb, 6) Frontal Mid. Orb, 7) Frontal Inf. Orb, 8) Frontal Sup. Medial, 9) Rectus, 10) Frontal Med. Orb., 11) Precentral, 12) Supp. Motor Area. In the Parietal region: 13) Paracentral Lobe, 14) Postcentral, 15) Parietal Sup., 16) Parietal Inf., 17) Supramarginal, 18) Angular. In the Occipital region: 19) Precuneus, 20) Cuneus, 21) Occipital Sup., 22) Occipital Mid., 23) Occipital Inf., 24) Lingual. In the Temporal region: 25) Temporal Sup., 26) Temporal Pole Sup., 27) Temporal Mid., 28) Temporal Pole Mid., 29) Temporal Inf, 30) Fusiform, 31) Parahippocampal. The Cerebellum, divided in: 32) Cerebellum Crus 1, 33) Cerebellum 3, 34) Cerebellum 4-5, 35) Cerebellum 6, 36) Cerebellum 7b, 37) Cerebellum 8, 38) Cerebellum 9, 39) Cerebellum 10. And additionally, the 40) Medulla, 41) Brain Stem and 42) Insula.

### III.2.2 Spherical Brain Mapping

In this section, the six measures proposed in Section II.2 will be analysed using a  $t$ -test. To proceed, a  $t$ -value will be computed for each pixel in the maps, yielding a significance map. These significance maps, or  $t$ -maps, are presented in Figure 7.

Absolute  $t$ -values higher than 1.96 can be considered to be significant, with a  $p < 0.05$ . In this case the areas of greater significance are in dark red and dark blue, where red is a positive  $t$ -value, meaning a higher value in controls than in AD subjects, and blue is a negative  $t$ -value, and conversely, blue means negative values, which are related to a higher value in AD than in controls.

The first thing to note is that the distribution of the  $t$  values in the Surface mapping, in both GM and WM, is not relevant at all, with very few significant pixels distributed along the whole image.

In the remaining GM mappings, greater  $t$ -values are located in the frontal, occipital and parietal lobes, but the most significant areas can be found in the temporal lobe. This is most obvious in the Average and Entropy mappings, but can also be found in Thickness. Number of Folds and Kurtosis present high, but however negative,  $t$ -values in these areas as well. This suggests that for GM, most of the neurodegeneration is located in the temporal lobe and all the underlying structures

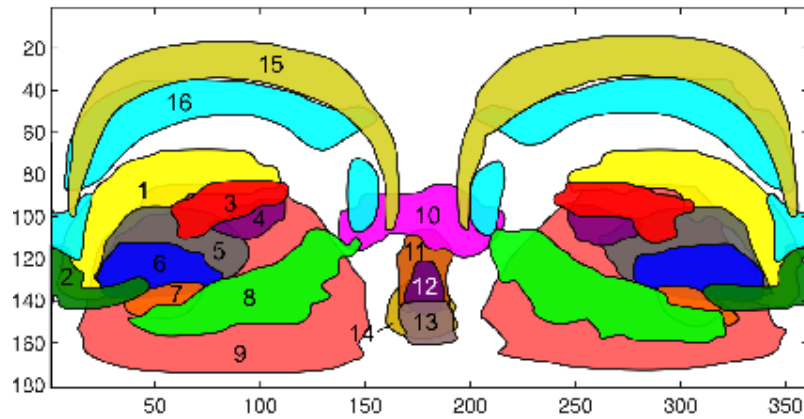


**Figure 6:** Projection of some important subcortical regions and organs. We observe the following subcortical structures: 1) Caudate Nucleus, 2) Olfactory Bulb, 3) Rolandic Operculum, 4) Heschl's gyri, 5) Putamen, 6) Globus Pallidus, 7) Amygdala, 8) Hippocampus, 9) Thalamus, 10) Lingual, 11) Vermis 4-5, 12) Vermis 7, 13) Vermis 9, 14) Vermis 1-2, 15) Cingulate Gyrus, 16) Corpus Callosum

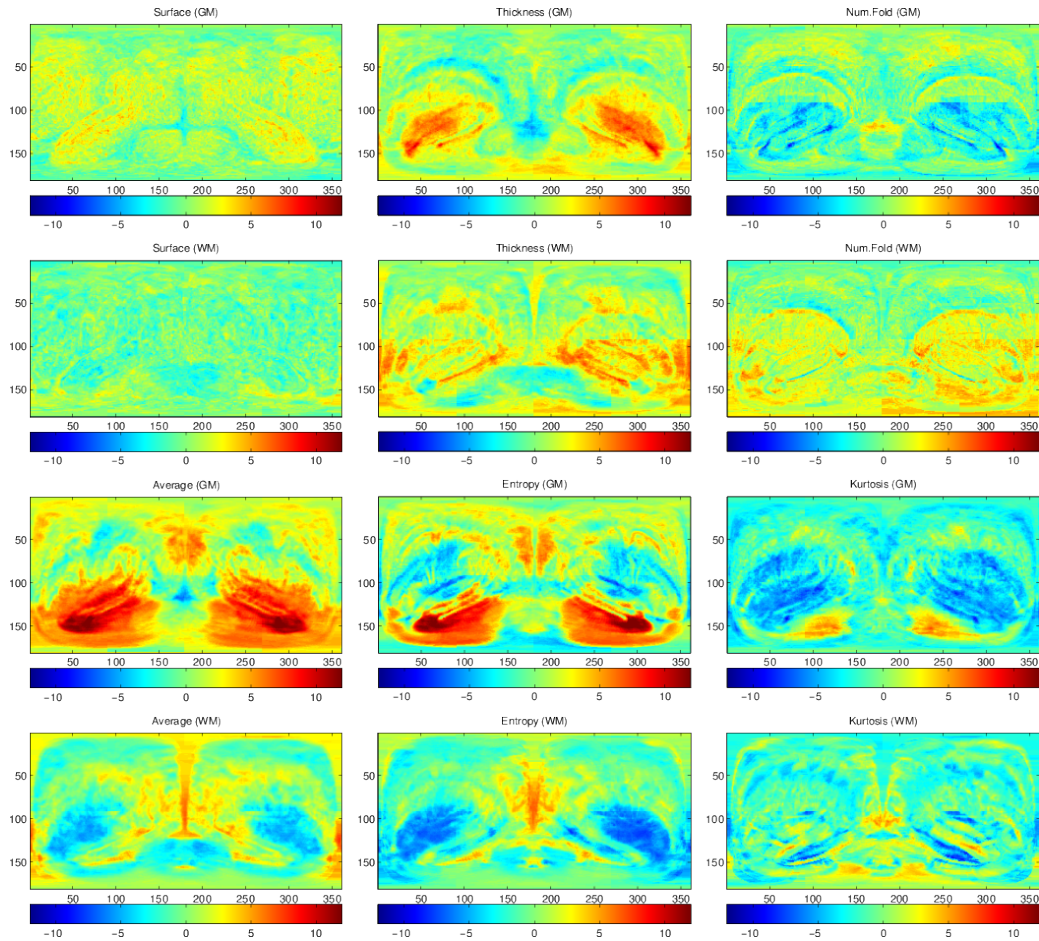


**Figure 7:** *t*-maps that present the level of statistical relevance in the AD vs. NC paradigm, for each type of mapping and GM and WM.

that are projected in this area, including the Hippocampus and Parahippocampal gyrus, which are considered a fundamental disease indicator in the NINCDS-ADRDA criteria [5]. Additionally, some structures that are located in the same area have been recently related to the progression of the disease, such as the Caudate Nucleus and Putamen [4]. These changes are more precisely located when using one of our spherical maps such as the Average or Entropy.

Conversely, in the WM mappings the selected regions are different. When using Number of Folds and Thickness, the selected areas are located in the vicinity of those obtained in GM. However, our spherical maps, especially Average and Entropy, behave differently. There is still high  $t$ -values that correspond to the White Matter of the Parahippocampal gyrus, but large areas of negative  $t$ -values that are located in areas corresponding to the Caudate Nucleus, Globus Pallidus and Putamen. The areas corresponding to the Posterior Cingulate gyrus and adjacent Precuneus present also values related to cell loss, as suggested in [2].

### III.2.3 Layered Extension

The significance levels of the layered mappings has been assessed as well. However, due to space restrictions, we will only analyse the anatomical features of one of the mappings: a four-layered average mapping of the GM, that can be checked in Figure 8.

It is plain to see that most of the neurological changes in GM appear in layers 2 and 3, specifically in the Hippocampus, Parahippocampal lobe and Amygdala (layer 2) and the temporal lobe (layer 3), where the values of the average mapping (equivalent to the density of the tissue) are higher in normal control subjects than in AD affected patients. This reveals atrophy in these organs, as it has been previously reported in the bibliography [5, 4]. In the case of WM, however, the changes are negative in the areas where the Rolandic Operculum, Heschl's gyri, Putamen and Globus Pallidus are found, and positive in some sections of the Hippocampus and the White Matter contained in the Parahippocampal lobe and the remaining parts of temporal lobe (layer 2 and 3). Nevertheless, the most significant differences are located in layer 1, in the borders between ventricles and Thalamus, and specially in the Cuneus, Precuneus and Posterior Cingulate gyrus, which were reported in [2].

### III.2.4 VRLBP

Finally, to end this statistical significance analysis, the  $t$ -maps of the more complex VRLBP mapping are presented in Figure 9.

These maps present low absolute  $t$  levels in most of the projection, however some small regions present high significance. These regions correspond to small areas in temporal lobe, Amygdala and Hippocampus in the GM, and even smaller regions in the WM corresponding to the limits between Hippocampus and Amygdala.

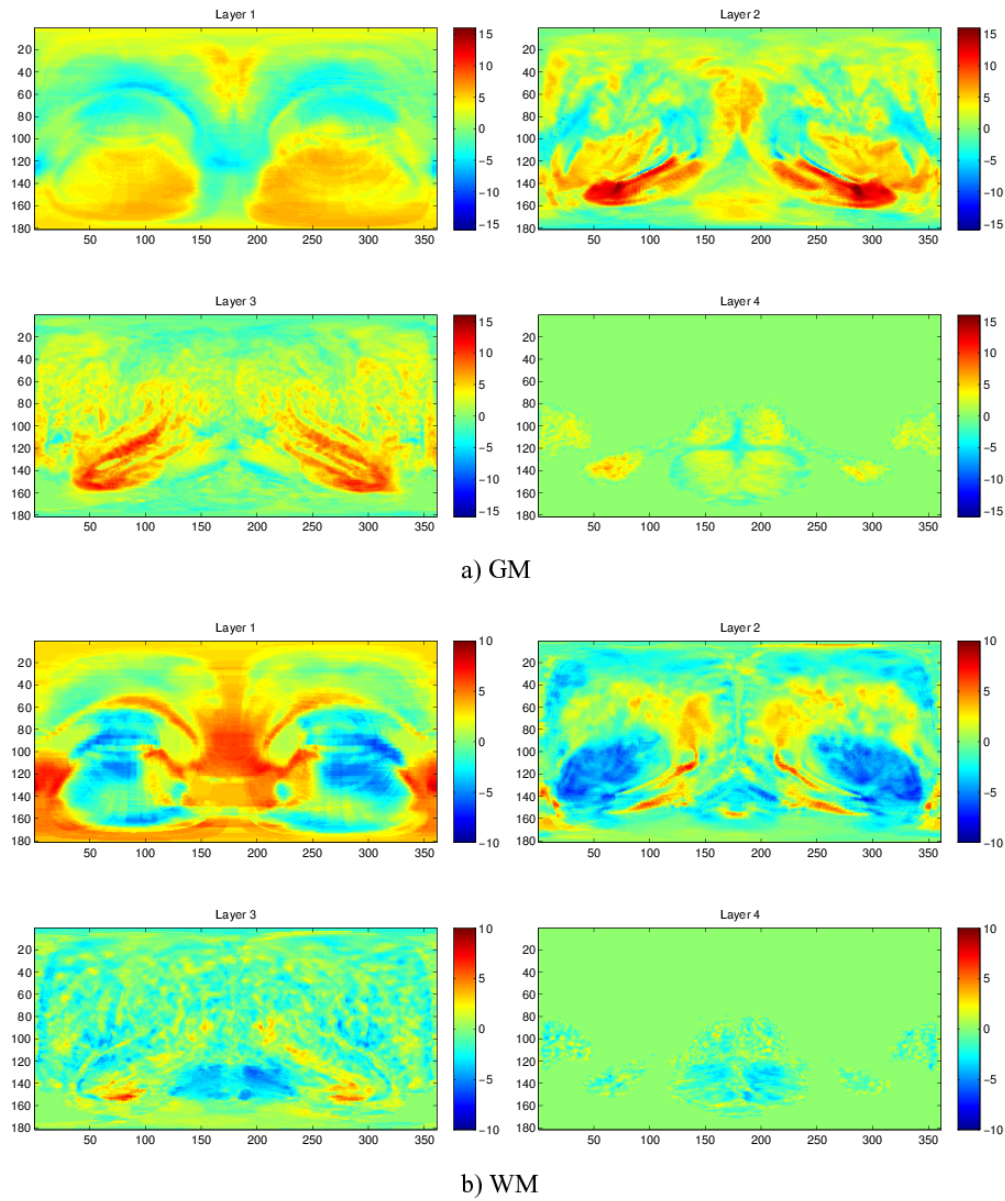


**Figure 8:** *t*-maps that present the level of statistical relevance in the AD vs. NC paradigm, for a four-layered average mapping over a) GM and b) WM.

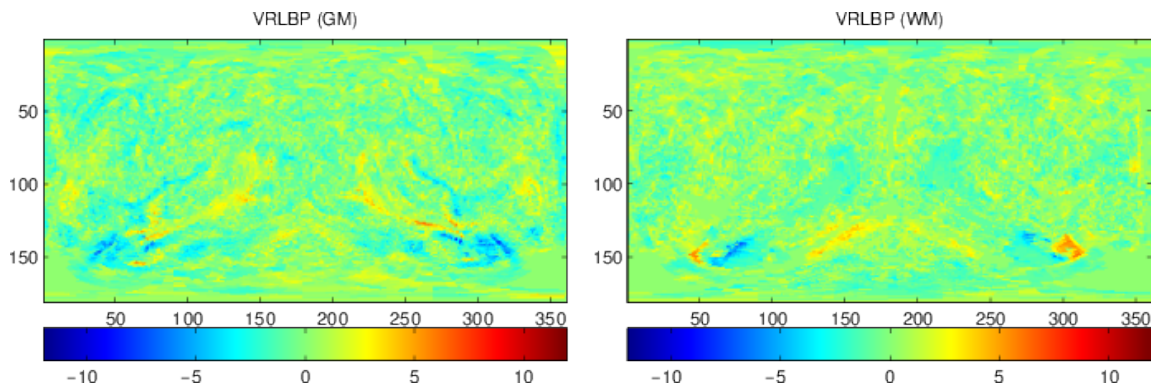


**Figure 9:** *t*-maps that present the level of statistical relevance in the AD vs. NC paradigm, for the VRLBP projections mapping over a) GM and b) WM.

### III.3. Classification Analysis

To obtain comparable performance metrics suitable to analyse the generalization capabilities of SBM, in this section a number of classification results are presented. A baseline is established in Section III.3.1 and then the performance of our maps, included the layered extension and VRLBP, is presented in Section III.3.2.

#### III.3.1 Baseline - VAF

In order to establish a baseline to assess the predictive ability of our maps, we will use the Voxels as Features (VAF) paradigm, described in [6]. This approach uses the whole 3D GM or WM segmented MR images and then uses all voxels of the 3D images as features in the SVM classification, yielding the performance values shown in Table 1. The performance of the SBM maps will be compared to these.

Approach	Accuracy	Sensitivity	Specificity
Vaf (GM)	$0.768 \pm 0.011$	$0.752 \pm 0.016$	$0.785 \pm 0.016$
Vaf (WM)	$0.642 \pm 0.009$	$0.668 \pm 0.012$	$0.617 \pm 0.013$

**Table 1:** Performance values (Average  $\pm$  Standard Deviation) for the Voxels as Features approach in both GM and WM tissues.

#### III.3.2 Spherical Brain Mapping

In this analysis, we have proceed as commented before, by computing the significance of each pixel using a *t*-test and then selecting a proportion of the most relevant, once they have been ranked according to their *t*-value. Later, these features are used to train and test a linear SVM classifier.

The results for each type of map are presented in Table 2, including the percentage of selected voxels (perc.) at which each value is obtained. Regarding the Grey Matter, we can observe that the best type of mappings in the diagnosis task, in terms of average accuracy, are the Average ( $0.879 \pm 0.005$ ) and Entropy ( $0.846 \pm 0.008$ ). There results are followed by the measures of Thickness ( $0.781 \pm 0.007$ ), Kurtosis ( $0.753 \pm 0.019$ ) and the worse accuracy estimates are for Number of Folds ( $0.749 \pm 0.013$ ) and Surface ( $0.638 \pm 0.006$ ).

Approach	Perc.	Accuracy	Sensitivity	Specificity
Surface (GM)	0.100	0.638 ± 0.006	0.660 ± 0.030	0.616 ± 0.024
Surface (WM)	0.100	0.672 ± 0.007	0.692 ± 0.018	0.652 ± 0.018
Thickness (GM)	0.725	0.781 ± 0.007	0.811 ± 0.011	0.751 ± 0.017
Thickness (WM)	0.925	0.758 ± 0.009	0.773 ± 0.017	0.744 ± 0.011
Num.Fold (GM)	0.600	0.749 ± 0.013	0.782 ± 0.019	0.716 ± 0.013
Num.Fold (WM)	0.500	0.757 ± 0.005	0.745 ± 0.006	0.768 ± 0.009
Average (GM)	0.575	0.879 ± 0.005	0.897 ± 0.006	0.861 ± 0.006
Average (WM)	0.150	0.800 ± 0.011	0.802 ± 0.013	0.798 ± 0.009
Entropy (GM)	0.825	0.846 ± 0.008	0.842 ± 0.009	0.849 ± 0.011
Entropy (WM)	0.525	0.796 ± 0.006	0.811 ± 0.009	0.781 ± 0.009
Kurtosis (GM)	1.000	0.753 ± 0.007	0.801 ± 0.011	0.704 ± 0.015
Kurtosis (WM)	0.175	0.697 ± 0.008	0.702 ± 0.018	0.693 ± 0.009
VRLBP (GM)	0.200	0.903 ± 0.010	0.890 ± 0.012	0.916 ± 0.018
VRLBP (WM)	0.150	0.909 ± 0.014	0.899 ± 0.028	0.919 ± 0.018

**Table 2:** Performance values (Average ± Standard Deviation) for the different SBM approaches.

In the case of White Matter, and according to Table 2, the performance is again higher in Average ( $0.800 \pm 0.011$ ) and Entropy ( $0.796 \pm 0.006$ ). Thickness and Number of Folds present similar, but lower, performance values, respectively  $0.758 \pm 0.009$  and  $0.757 \pm 0.005$ , and being the Kurtosis ( $0.697 \pm 0.008$ ) and Surface ( $0.672 \pm 0.007$ ) maps the less powerful.

However, VRLBP outperform all these approaches by obtaining an accuracy of  $0.903 \pm 0.010$  for GM and  $0.909 \pm 0.014$  for WM, revealing itself as the best technique.

The evolution of the performance of the maps as the number of selected pixels varies is shown in Figure 10. In general, it is possible to see very small differences in the accuracy of the system, which makes its performance almost independent from the number of selected pixels. However, this is not the case of the Surface, and, more remarkable, the VRLBP. In the latter, the performance is the best for both tissues when the proportion of selected pixels is small, but degrades significantly as its number increases.

Regarding the four-layer extension to SBM, the performance values obtained by different mappings at different layers and thresholds ( $t$ -values of 2, 4, 8 and 10) is presented in Figure 11.

The first thing that we can observe is that for both GM and WM tissues, the better performance is achieved with the second layer. This is specially surprising in the WM case, as the highest  $t$ -values were located in layer 1.

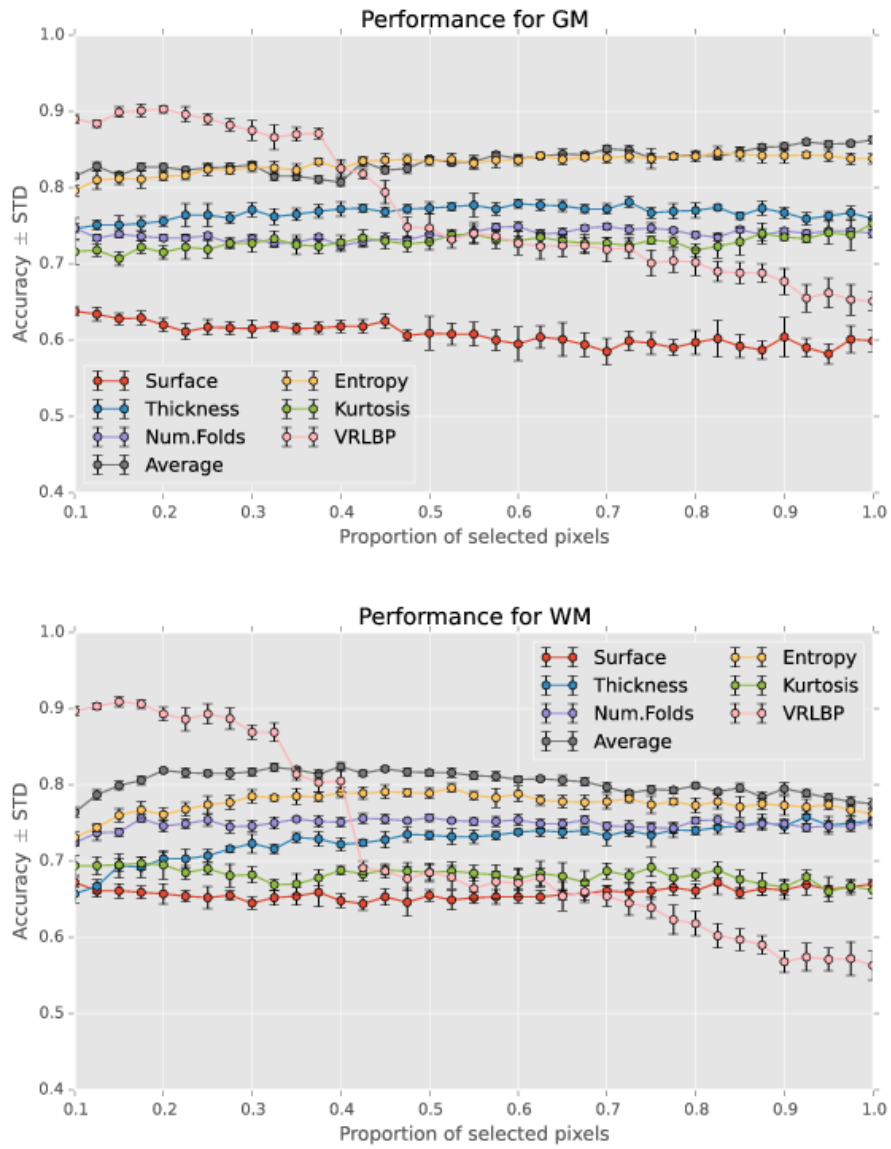


**Figure 10:** Performance for the different SBM approaches over the: a) Grey Matter and b) White Matter.

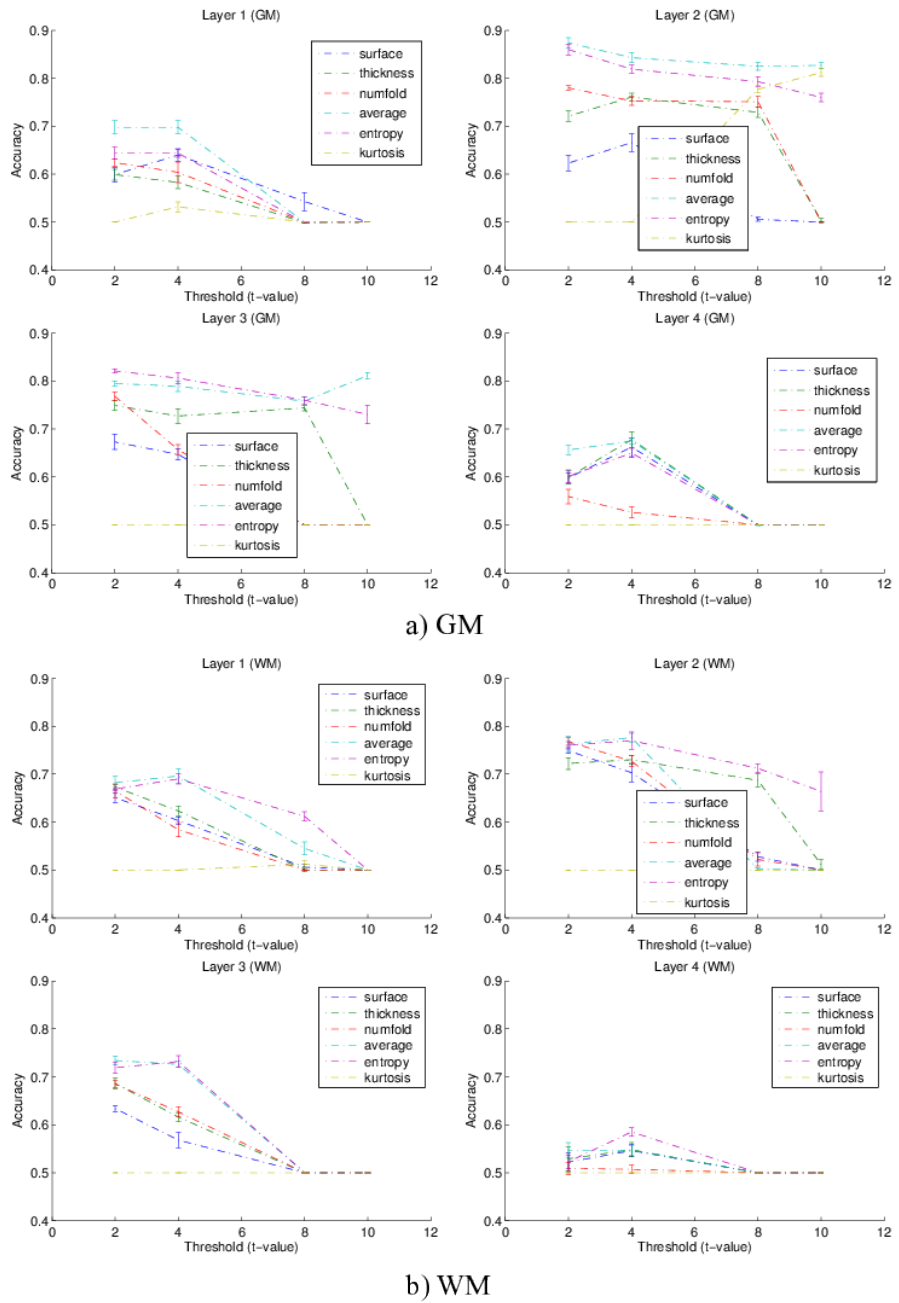


**Figure 11:** Performance for the different four-layered mappings over the: a) Grey Matter and b) White Matter at different levels of statistical significance.

#### IV. DISCUSSION

The structural changes in MR images during the progression of the Alzheimer's Disease are widely documented in the bibliography [3, 2, 4, 6, 9, 10]. According to our current knowledge, the neurodegeneration and posterior atrophy occurs mainly in the GM tissue, although significant changes are present also in WM.

The mappings defined throughout Sections II.2, II.3 and II.4 account for different properties of the tissues crossed by  $v_{\theta,\varphi}$ . As it can be seen in Figure 12, our mappings show in general a higher performance when using the GM tissue, which is consistent with the literature. There are some exceptions, however, being the clearest the VRLBP, and, to a lesser extent, the number of folds and surface. The different mappings and their utility will be described in the following paragraphs.

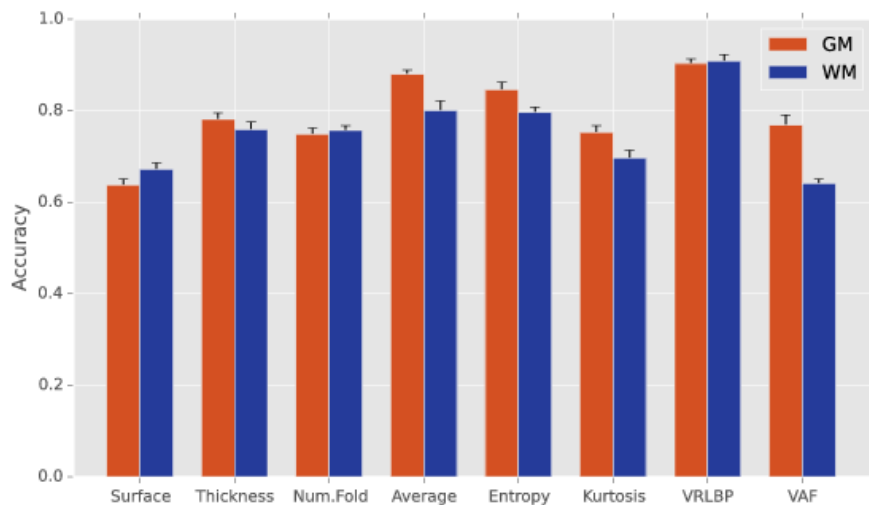


**Figure 12:** Performance at the operation point for the different mappings over the Grey Matter and White Matter, compared with the performance of VAF.

The first three approaches, Surface, Thickness and Number of Folds are easily interpreted, as they intend to represent the surface of the tissue by mapping the distance between the centre of the image and the last voxel, the thickness of the tissue, and a measure of the complexity of the different sulci and gyri.

Surface and Thickness are highly related to other measures provided by widely-used software. However, as they are related to our more general SBM description, their performance is poor, specially in the case of the Surface mapping. As it can be seen in Fig. 3, and later in the  $t$ -maps at Fig. 7, the detail of the surface map lacks higher detail, specially due to the superposing gyri and sulci. These superposition occur to a lesser extent in WM tissue, and this is probably why this technique obtains higher performance in WM than in GM.

As for the case of Thickness, although similar, it gathers much more information than the surface, without achieving, however, the level of detail of the cortical thickness measures provided by Freesurfer [10] or other software. Nevertheless, cortical thickness it is a descriptive, widely accepted as a measure of neurodegeneration in Alzheimer's Disease in the literature [9, 10], and its measures might be relevant for a subsequent analysis.

Number of Folds, however, is intended to model the complexity of the cerebral cortex, and

therefore, it is of far more use in the case of GM than in the WM. This can be easily checked when looking at the maps obtained for both GM and WM in Figure 3.

The last three measures described in Section II.2 are statistical values that describe the variability of the sampling set  $V_{\theta,\varphi}$ . It would be reasonable to expect the better performance to be linked to the mapping that better models the tissue atrophy.

This is the case of the average of these intensities, which can be interpreted as the total amount of tissue, being therefore a good measure of the level of brain atrophy in each direction  $(\theta, \varphi)$ . The average maps show the best performance of all the measures proposed in Section II.2, and is higher in GM than in WM. This is consistent with the literature, as atrophy mainly occurs in GM tissues.

Entropy is a more complex statistical concept that comes from information theory, but is usually related to the amount of information, or in other words, the “randomness” of a source. In our particular case it could be interpreted as a measure of texture, that is, the grey-level variability in the direction of  $\mathbf{v}_{\theta,\varphi}$ . These maps perform very similar to the average ones in both GM and WM, suggesting that the entropy accounts for the tissue density as well.

The last mapping defined, Kurtosis, is a fourth-order statistic, often interpreted as the peakedness (width of peak) of a probability distribution. In our context, it is related to the sharpness of the changes in the direction of  $\mathbf{v}_{\theta,\varphi}$ , and thus is related to the number of folds. As in the case of the latter, the Kurtosis performs poorly in both types of tissues, probably because they are measures that are not as directly related to atrophy as other measures such as average, entropy or thickness.

The last of the single measures proposed in this work is the Volumetric Radial LBP defined in Section II.4. It is a measure of the texture not only in the direction of  $\mathbf{v}_{\theta,\varphi}$ , but also in the neighbourhood of the mapping vector. Therefore, it is not strange that it obtains the best performance of the whole work, yielding accuracy results above 0.9 for both GM and WM tissues.

This could seem counter-intuitive, as the  $t$ -maps for this technique, presented in Fig. 9, show small regions of high significance, when compared to the measures in Sec. II.2. Yet, despite its size, it performs fairly well with a relatively small amount of data. It is probably due to the nature of VRLBP, and the areas highlighted in Fig. 9 probably correspond to the texture changes associated to the loss of tissue in the Hippocampus.

As for the layered extension, which might seem a powerful method to add detail to the mappings, obtains however similar performance to the methodology above. It seems that the amount of information that can be obtained by each measure does not depend on the number of layers, and accordingly, its benefits are only related to visualization. In this case, best values are obtained in layer 2, which is consistent to the presence of some organs, specially the Hippocampus.

Finally, in order to have another look at the performance of our mappings, the ROC curves of each type are presented in Figure 13. There we can see how the VRLBP approach outperforms all the other measures, specially in the case of WM tissue. In GM, Average and Entropy present values really close to VRLBP, as expected. Conversely, the poorest performance is achieved by the Kurtosis and Surface mappings, however the Surface performs better in WM than in GM. These results confirm the performance values presented in Table 2 and Figure 10, making our proposed mapping framework a reasonable choice for obtaining both a visual interpretation of otherwise hidden features and a significant dimensionality reduction.

It is important to note that our Spherical Brain Mapping defines a whole framework that can be easily extended with different sampling strategies. This is the case of the layered extension and the helical sampling in VRLBP, but they are only two examples of what can be done. Since our simplest approach implies a computation of a value from a vector of intensities, measures used to describe time-course data could be added to complete and highlight different properties of the tissues. In this context, high-order statistics [26], as well as spectral measures [27] have

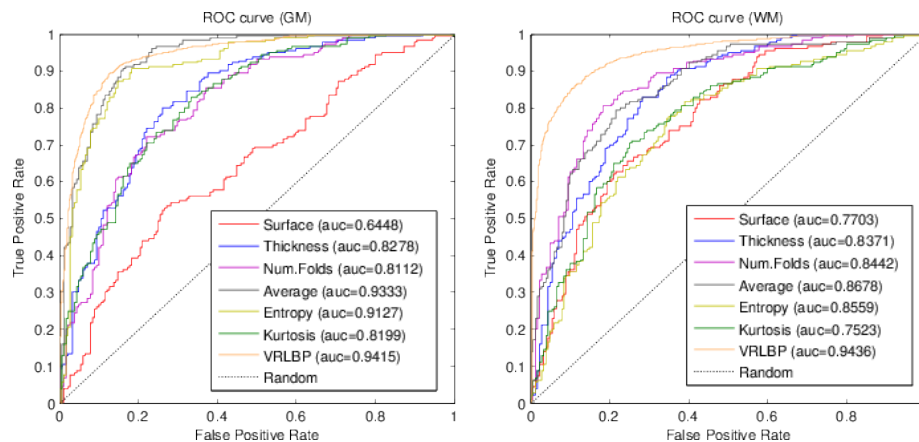


**Figure 13:** ROC curves of the different mappings for the GM and WM tissues.

been successfully applied to analyse electroencephalogram (EEG) signals, and could be therefore applied here to bring different structural properties of the images into focus. Additionally, our mapping method is potentially applicable to other imaging modalities, such as PET and SPECT, where the structural information is sometimes lost [12, 17]. Our technique does not need the use of complex co-registering of MRI and functional imaging to locate cerebral structures, as it rely only in their angle and depth. Moreover, in the case of Diffusion Tensor Imaging (DTI), which has proven itself as a good tool for the diagnosis of Alzheimer's Disease [28, 29], SBM could be modified to replace  $v_i$  with each tract, and subsequently project a given feature, resulting in a summary of the tract's behaviour in a single two-dimensional image.

## V. CONCLUSIONS

In this work the Spherical Brain Mapping (SBM), a new framework for feature reduction, visualization and analysis of Magnetic Resonance Imaging (MRI) is presented. It is based on a mapping from 3D spherical coordinates to a 2D map that contains different structural and statistical measures. Some of the measures are highly related to typical changes in the brain (atrophy, decrement in cortical thickness), that have been already successfully tested in the diagnosis task.

This new strategy allows both a visual interpretation of different brain features using two-dimensional maps and a subsequent computational processing that could be used to obtain objective measures to help physicians in the diagnosis task. Different SBM measures have been tested in combination with  $t$ -value maps (used to select the most relevant pixels in the maps) in an automatic classification procedure using Alzheimer's Disease affected patients (AD) versus Normal Controls (NC). In this case, some of the maps yielded high performance values, matching and even outperforming well-established methodologies in the field, but with the addition of a significant computational load reduction. Furthermore, with the addition of a four-layered mapping, in which different structures of the brain are displayed at different depths, the system kept these good performance values, while providing a better visual interpretation of the results.

However, the first approach described in this paper is the simplest one that could be stated -only a feature selection step has been added in the evaluation of the mappings-, with the only addition of the layered approach. In future works, the SBM framework could be expanded by adding different types of measures to the set, and the processing pipeline can be improved by processing the different maps using univariate or multivariate algorithms to make the most of the

information contained within.

#### ACKNOWLEDGEMENTS

This work was partly supported by the MICINN under the TEC2008-02113 and TEC2012-34306 projects and the Consejería de Economía, Innovación, Ciencia y Empleo (Junta de Andalucía, Spain) under the Excellence Projects P09-TIC-4530 and P11-TIC-7103, as well as the “Programa de fortalecimiento de las capacidades de I+D+I en las Universidades 2014-2015”, cofunded by the European Regional Development Fund (ERDF) under Project FC14-SAF-30.

Data collection and sharing for this project was funded by the Alzheimer’s Disease Neuroimaging Initiative (ADNI) (National Institutes of Health Grant U01 AG024904) and DOD ADNI (Department of Defense award number W81XWH-12-2-0012). ADNI is funded by the National Institute on Aging, the National Institute of Biomedical Imaging and Bioengineering, and through generous contributions from the following: AbbVie, Alzheimers Association; Alzheimers Drug Discovery Foundation; Araclon Biotech; BioClinica, Inc.; Biogen; Bristol-Myers Squibb Company; CereSpir, Inc.; Eisai Inc.; Elan Pharmaceuticals, Inc.; Eli Lilly and Company; EuroImmun; F. Hoffmann-La Roche Ltd and its affiliated company Genentech, Inc.; Fujirebio; GE Healthcare; IXICO Ltd.; Janssen Alzheimer Immunotherapy Research & Development, LLC.; Johnson & Johnson Pharmaceutical Research & Development LLC.; Lumosity; Lundbeck; Merck & Co., Inc.; MesoScale Diagnostics, LLC.; NeuroRx Research; Neurotrack Technologies; Novartis Pharmaceuticals Corporation; Pfizer Inc.; Piramal Imaging; Servier; Takeda Pharmaceutical Company; and Transition Therapeutics. The Canadian Institutes of Health Research is providing funds to support ADNI clinical sites in Canada. Private sector contributions are facilitated by the Foundation for the National Institutes of Health ([www.fnih.org](http://www.fnih.org)). The grantee organization is the Northern California Institute for Research and Education, and the study is coordinated by the Alzheimer’s Disease Cooperative Study at the University of California, San Diego. ADNI data are disseminated by the Laboratory for Neuro Imaging at the University of Southern California.

The code for the SBM algorithm can be found found at <http://wdb.ugr.es/~fjesusmartinez/portfolio/sbm/>.

#### REFERENCES

- [1] Alzheimer’s Disease International. The global impact of dementia 2013–2050. Technical report, London: Alzheimer’s Disease International, London: Alzheimer’s Disease International., 2013.
- [2] J. C. Baron, G. Chételat, B. Desgranges, G. Percey, B. Landeau, V. de la Sayette, and F. Eustache. In vivo mapping of gray matter loss with voxel-based morphometry in mild alzheimer’s disease. *Neuroimage*, 14(2):298–309, Aug 2001.
- [3] Chandan Misra, Yong Fan, and Christos Davatzikos. Baseline and longitudinal patterns of brain atrophy in MCI patients, and their use in prediction of short-term conversion to AD: Results from ADNI. *NeuroImage*, 44(4):1415–1422, February 2009.
- [4] Michela Pievani, Martina Bocchetta, Marina Boccardi, Enrica Cavedo, Matteo Bonetti, Paul M. Thompson, and Giovanni B. Frisoni. Striatal morphology in early-onset and late-onset alzheimers disease: a preliminary study. *Neurobiology of Aging*, 34(7):17281739, Jul 2013.
- [5] Bruno Dubois, Howard H Feldman, Claudia Jacova, Steven T DeKosky, Pascale Barberger-Gateau, Jeffrey Cummings, Andr Delacourte, Douglas Galasko, Serge Gauthier, Gregory Jicha,

- and et al. Research criteria for the diagnosis of alzheimers disease: revising the nincdsadrda criteria. *The Lancet Neurology*, 6(8):734746, Aug 2007.
- [6] J. Stoeckel, N. Ayache, G. Malandain, P. M. Koulibaly, K. P. Ebmeier, and J. Darcourt. Automatic Classification of SPECT Images of Alzheimer’s Disease Patients and Control Subjects. In *Medical Image Computing and Computer-Assisted Intervention - MICCAI*, volume 3217 of *Lecture Notes in Computer Science*, pages 654–662. Springer, 2004.
- [7] Fatma Polat, Selcuk Orhan Demirel, Omer Kitis, Fatma Simsek, Damla Isman Haznedaroglu, Kerry Coburn, Emre Kumral, and Ali Saffet Gonul. Computer based classification of mr scans in first time applicant alzheimer patients. *Curr Alzheimer Res*, 9(7):789–794, Sep 2012.
- [8] J. M. Górriz, A. Lassel, J. Ramírez, D. Salas-Gonzalez, C. G. Puntonet, and E. W. Lang. Automatic selection of ROIs in functional imaging using Gaussian mixture models. *Neuroscience Letters*, 460(2):108–111, 2009.
- [9] Xiao Han, Jorge Jovicich, David Salat, Andre van der Kouwe, Brian Quinn, Silvester Czanner, Evelina Busa, Jenni Pacheco, Marilyn Albert, Ronald Killiany, et al. Reliability of mri-derived measurements of human cerebral cortical thickness: the effects of field strength, scanner upgrade and manufacturer. *Neuroimage*, 32(1):180–194, 2006.
- [10] Bruce Fischl, André van der Kouwe, Christophe Destrieux, Eric Halgren, Florent Ségonne, David H Salat, Evelina Busa, Larry J Seidman, Jill Goldstein, David Kennedy, et al. Automatically parcellating the human cerebral cortex. *Cerebral cortex*, 14(1):11–22, 2004.
- [11] Diego Salas-Gonzalez, Juan M. Górriz, Javier Ramírez, Miriam López, Ignacio A. Illan, Fermín Segovia, Carlos G. Puntonet, and Manuel Gómez-Río. Analysis of SPECT brain images for the diagnosis of Alzheimer’s disease using moments and support vector machines. *Neuroscience Letters*, 461:60–64, September 2009.
- [12] I. A. Illán, J. M. Górriz, J. Ramírez, D. Salas-González, M. López, F. Segovia, P. Padilla, and C. G. Puntonet. Projecting independent components of SPECT images for computer aided diagnosis of Alzheimer’s disease. *Pattern Recognition Letters*, 31(11):1342–1347, August 2010.
- [13] Darya Chyzhyk, Manuel Graña, Alexandre Savio, and Josu Maiora. Hybrid dendritic computing with kernel-lica applied to Alzheimer’s disease detection in MRI. *Neurocomputing*, 75(1):7277, Jan 2012.
- [14] Francisco Jesús Martínez-Murcia, JM Górriz, Javier Ramírez, Carlos García Puntonet, and IA Illán. Functional activity maps based on significance measures and independent component analysis. *Computer methods and programs in biomedicine*, 111(1):255–268, 2013.
- [15] J. M. Górriz, J. Ramírez, A. Lassel, D. Salas-Gonzalez, E. W. Lang, C. G. Puntonet, I. Álvarez, M. López, and M. Gómez-Río. Automatic computer aided diagnosis tool using component-based SVM. In *IEEE Nuclear Science Symposium Conference Record, Medical Imaging Conference, Dresden, Germany.*, pages 4392–4395. IEEE-NSS, 2008.
- [16] Andrés Ortiz, Juan M. Górriz, Javier Ramírez, and F.J. Martínez-Murcia. Lvq-SVM based CAD tool applied to structural MRI for the diagnosis of the alzheimers disease. *Pattern Recognition Letters*, 34(14):17251733, Oct 2013.
- [17] J. Ramírez, J. M. Górriz, R. Chaves, M. López, D. Salas-González, I. Álvarez, and F. Segovia. SPECT image classification using random forests. *Electronics Letters*, 45:604–605, 2009.

- [18] Francisco Jesús Martínez-Murcia, Juan Manuel Górriz, Javier Ramírez, Ignacio Alvarez Illán, Diego Salas-González, Fermín Segovia, and Alzheimer's Disease Neuroimaging Initiative . Projecting mri brain images for the detection of alzheimer's disease. *Stud Health Technol Inform*, 207:225–233, 2015.
- [19] K.J. Friston, J. Ashburner, S.J. Kiebel, T.E. Nichols, and W.D. Penny. *Statistical Parametric Mapping: The Analysis of Functional Brain Images*. Academic Press, 2007.
- [20] Luders E, Gaser C, Jäncke L, Schlaug G A voxel-based approach to gray matter asymmetries. *Neuroimage*, 22:656–664, 200.
- [21] Ojala, T., Pietikäinen, M., Harwood, D.: A comparative study of texture measures with classification based on featured distributions. *Pattern Recognition* 29(1) (January 1996) 51–59
- [22] Zhao, G., Pietikainen, M.: Dynamic texture recognition using local binary patterns with an application to facial expressions. *IEEE Trans. Pattern Anal. Mach. Intell.* 29(6) (June 2007) 915–928
- [23] R Kohavi. A study of cross-validation and bootstrap for accuracy estimation and model selection. In *Proceedings of International Joint Conference on AI*, pages 1137–1145, 1995.
- [24] C. C. Chang and C. J. Lin. LIBSVM: a library for support vector machines. Technical report, Dept. of Computer Science and Information Engineering, National Taiwan University, 2001.
- [25] N. Tzourio-Mazoyer, B. Landeau, D. Papathanassiou, F. Crivello, O. Etard, N. Delcroix, B. Mazoyer, and M. Joliot. Automated anatomical labeling of activations in spm using a macroscopic anatomical parcellation of the mni mri single-subject brain. *Neuroimage*, 15(1):273–289, Jan 2002.
- [26] Shang-Ming Zhou, John Q. Gan, and Francisco Sepulveda. Classifying mental tasks based on features of higher-order statistics from EEG signals in braincomputer interface. *Information Sciences*, 178(6):16291640, Mar 2008.
- [27] T. Locatelli, M. Cursi, D. Liberati, M. Franceschi, and G. Comi. EEG coherence in alzheimers disease. *Electroencephalography and Clinical Neurophysiology*, 106(3):229237, Mar 1998.
- [28] M. Graña, M. Termenon, A. Savio, A. Gonzalez-Pinto, J. Echeveste, J.M. Pérez, and A. Besga. Computer aided diagnosis system for alzheimer disease using brain diffusion tensor imaging features selected by pearsons correlation. *Neuroscience Letters*, 502(3):225229, Sep 2011.
- [29] David A. Medina and Moises Gaviria. Diffusion tensor imaging investigations in alzheimer's disease: the resurgence of white matter compromise in the cortical dysfunction of the aging brain. *Neuropsychiatr Dis Treat*, 4(4):737–742, Aug 2008.